The Mean-Square Slope of Ocean Surface Waves and Its Effects on Radar Backscatter

YUGUANG LIU

College of Marine Studies, University of Delaware, Newark, Delaware

MING-YANG SU

Oceanography Division, Naval Research Laboratory, Stennis Space Center, Mississippi

XIAO-HAI YAN

College of Marine Studies, University of Delaware, Newark, Delaware

W. TIMOTHY LIU

Jet Propulsion Laboratory, California Institute of Technology, Pasadena, California

(Manuscript received 23 March 1998, in final form 12 October 1999)

ABSTRACT

The mean-square slope (MSS) of the sea surface for upwind and crosswind is derived, based on Phillips' equilibrium spectrum and the model herein on gravity–capillary wave spectrum. The MSS integrated from the above two spectra over high-frequency dissipation length (1 mm) fits the optical observations very well. The radar backscatter cross section (RBCS), calculated from specular reflection theory using the Ku-band filtered MSS, is in keeping with the empirically based Ku-band models by Brown for the *GEOS-3* 13.9-GHz altimeter, and by Witter and Chelton for the Geosat 13.5-GHz altimeter. Also, the RBCS, calculated using the C-band filtered MSS, is in keeping with the *ERS-1/-2* scatterometer empirically based algorithms CMOD3 and CMOD4.

The physics included in this model on gravity–capillary wave spectrum is also illustrated. The short-wave dissipation due to wave–drift interactions has the effect of suppressing the spectral density at high wind condition, which further influences the directional spreading rate. This effect can be denoted by c^2/U_{10}^2 or c^2/c_p^2 dependence of short-wave spectrum. It is suggested that the k_p/k dependence observed in the range of gravity waves should not be extended to the region of short waves. The parasitic capillary wave dissipation due to molecular viscosity can be balanced by the energy supply from the underlying waves, hence it is removed from the model. The eddy viscosity is due to turbulence at the wind-drift layer, which suppresses the spectrum of high-frequency waves with wavelengths on the order of millimeters.

1. Introduction

A knowledge of the ocean surface slope distribution and the mean-square slope (MSS) is essential to understanding the radar backscatter at or away from normal incidence (Liu and Pierson 1994; Liu and Yan 1995; Liu 1996; Liu et al. 1997). The radar backscatter cross section (RBCS) due to specular reflection is (Barrick 1968; Valenzuela 1978; Donelan and Pierson 1987; Brown 1990; Apel 1994)

$$\sigma_o(\theta) = \pi \sec^4\theta f(\zeta_x, \zeta_y)|R(0)|^2, \qquad (1)$$

where θ is the radar incidence angle and $|R(0)|^2$ is the Fresnel reflection coefficient for normal incidence (Schanda 1976). In (1), $f(\zeta_x, \zeta_y)$ is the probability density function (PDF) of ocean surface slope at the specular points, where ζ is the surface elevation, and ζ_x and ζ_y are the slope components for upwind and crosswind. For the range of small slope or the range near normal incidence, the PDF of surface slope can be approximated by

$$f(\zeta_x, \zeta_y) = \frac{1}{2\pi\sigma_u\sigma_c}\exp\left[-\frac{1}{2}\left(\frac{\zeta_x^2}{\sigma_u^2} + \frac{\zeta_y^2}{\sigma_c^2}\right)\right], \qquad (2)$$

where σ_u^2 and σ_c^2 represent the upwind and crosswind MSS components, respectively. The Gram–Charlier distribution can improve the Gaussian distribution for a little higher accuracy only in the range of small slope. For the range of large slope, which corresponds to larger incidence angles away from the normal incidence, it is

Corresponding author address: Dr. Yuguang Liu, College of Marine Studies, University of Delaware, Newark, DE 19716.
E-mail: yuguang@newark.cms.udel.edu

found that both the Gaussian and the Gram–Charlier distributions fail to describe the PDF of ocean surface slope (Liu et al. 1997). A more appropriate PDF derived by Liu et al. (1997) is

$$f(\zeta_x, \zeta_y) = \frac{n}{2\pi(n-1)\sigma_u\sigma_c} \times \left[1 + \frac{\zeta_x^2}{(n-1)\sigma_u^2} + \frac{\zeta_y^2}{(n-1)\sigma_c^2}\right]^{-(n+2)/2}, \quad (3)$$

where n is the peakedness coefficient. The skewness has been ignored in (3) because of its very small order. When $n = 10$, the proposed PDF fits the Gram–Charlier distribution of Cox and Munk (1954a,b) very well in the range of small slope ($\zeta_x < 2.5\sigma_u$ and $\zeta_y < 2.5\sigma_c$). For a nadir-looking altimeter, that is, the incidence angle θ being zero, we have from (1) and (2)

$$\sigma_o(0) = \frac{|R(0)|^2}{2\sigma_u\sigma_c}. \quad (4)$$

From (1) and (3), we obtain

$$\sigma_o(0) = \frac{n}{n-1}\frac{|R(0)|^2}{2\sigma_u\sigma_c}. \quad (5)$$

Often, we express σ_o in decibels, σ_o (dB) $= 10 \log_{10}(\sigma_o)$. From (4), the RBCS in decibels is

$$\sigma_o(\text{dB}) = 10 \log_{10}(|R(0)|^2) - 10 \log_{10}(2\sigma_u\sigma_c). \quad (6)$$

From (5), the RBCS in decibels is

$$\sigma_o(\text{dB}) = 10 \log_{10}(|R(0)|^2) + 10 \log_{10}\left(\frac{n}{n-1}\right) - 10 \log_{10}(2\sigma_u\sigma_c). \quad (7)$$

For a smooth surface, the normal incidence Ku-band and X-band Fresnel reflectivity $|R(0)|^2 = 0.62$ (Wu 1994; Liu 1996) and $10 \log_{10}(|R(0)|^2) = -2.1$ dB. In the real surface with small structure, there is a discrepancy between the Fresnel reflectivity and the effective reflection coefficient (Valenzuela 1978; Masuko et al. 1986; Jackson et al. 1992). A calibration for $10 \log_{10}|R(0)|^2$ in (6) and (7) is needed. Wu (1994) suggested a value of -2.1 dB for the calibration. The discrepancy is probably due to unmodeled scattering processes, for example, spray, foam absorption, etc. Adopting Wu's suggestion, (6) and (7) become

$$\sigma_o(\text{dB}) = -4.2(\text{dB}) - 10 \log_{10}(2\sigma_u\sigma_c) \quad (8)$$

for a rough surface of Gaussian statistics, and

$$\sigma_o(\text{dB}) = -4.2(\text{dB}) + 10 \log_{10}\left(\frac{n}{n-1}\right) - 10 \log_{10}(2\sigma_u\sigma_c), \quad (9)$$

for a rough surface of the statistics of Liu et al. (1997). To apply (8) or (9) to the ocean, only a portion of the MSS should be included. According to Valenzuela (1978) and Liu et al. (1997), only the ocean waves whose wavelengths are significantly longer than the radar wavelength make contribution to the measured MSS.

Many efforts have been undertaken to investigate the MSS. For X-band ($\lambda = 2.5$ cm) filtered MSS, Wu (1994) suggests

$$\sigma^2 = \sigma_u^2 + \sigma_c^2 = 0.0090 + 0.012 \ln(U_{10}). \quad (10)$$

based on the observations of Cox and Munk (1954a,b) when $U_{10} < 7$ m s^{-1}. Based on the comparisons of the RBCS calculated from specular reflection theory with the measurements of C-band, X-band, Ku-band, and Ka-band microwave radars, an averaged MSS is suggested by Apel (1994):

$$\sigma^2 = \sigma_u^2 + \sigma_c^2 = 0.004U_{10}. \quad (11)$$

The MSS obtained by Masuko et al. (1986) and Jackson et al. (1992) is the part contributed by gravity waves. Jackson et al. (1992) used their derived MSS to determine the Phillips constant in the equilibrium range. In their papers, the MSS contributed by the shorter waves is regarded as small structure and their effect on radar backscatter is included in the effective reflection coefficient, due to their special mathematical approach. The comparison shows (not included in this paper) that the derived MSS by Jackson (1991) and Jackson et al. (1992) is equal to our MSS for k up to 100 rad m^{-1}. The MSS has also been derived from the ocean surface spectra (Donelan and Pierson 1987; Apel 1994). Their derived values are much higher than the observations of Cox and Munk (1954a,b), and much higher than the values required in (8). An optical sensor can detect water wave slopes generated by arbitrarily short water waves up to the wavelength of reflected light, while microwave radar can only measure a part of the surface slopes up to the radar wavelength. How to obtain a reasonable estimate for the MSS in a wider range of wavenumber is the main subject from section 2 through section 6. The involved physics and arguments are given in section 7.

2. MSS of gravity–capillary waves

In consideration of energy dissipation, wave–drift interaction, and long-wave modulation, a model of the gravity–capillary wave spectrum is suggested (Liu 1996; Liu and Yan 1995) as follows:

$$\Phi_w(k, \phi) = mk^{-4}\left(\frac{u_* - \delta}{c}\right)^2 \times \left[1 - \exp\left(-\frac{c^2}{\alpha_1 U_{10}^2}\right)\right] D(\phi) D_e, \quad (12)$$

with the directional spreading function of gravity–capillary waves given by

$$D(\phi) = \frac{1 - \exp\left[-\dfrac{c^2}{(\alpha_1 \cos^2\phi + \alpha_2 \sin^2\phi)U_{10}^2}\right]}{1 - \exp\left(-\dfrac{c^2}{\alpha_1 U_{10}^2}\right)} \operatorname{sech}^2(h\phi), \tag{13}$$

where m is a constant, u_* is the wind friction velocity, δ is the threshold wind friction velocity, c is the wave phase speed, and α_1 and α_2 are the dissipation coefficients due to wave–drift interaction.

In (12), D_e is called the eddy viscosity and generated by turbulence at wind–drift layer. Here, $D_e = \exp[-\alpha_e k^{2.5} (u_* - \delta)^{-0.75}]$, where the coefficient α_e is determined to be 0.0011 (cm rad^{-1})$^{2.5}$ (cm s^{-1})$^{0.75}$, based on the image slope gauge laboratory measurement (Klinke and Jähna 1992, see their Fig. 3: fetch = 28.9 m, U_{10} = 2–10 m s^{-1}), the filed measurement (Klinke and Jähna 1995, see their Fig. 6(b): field data, U_{10} = 4.0–6.0 m s^{-1}), and the laser slope gauge laboratory measurement of Jähna and Riemer (1990, see their Fig. 7: fetch = 90 m, U_{10} = 2.7–17.2 m s^{-1}).

Other parameters are $m = 1/320$, $h = 1.3$, $\delta = 5$ cm s^{-1}, $\alpha_2 = 0.000\,05$, $\alpha_1 = 0.0002$ for the leeward side of background waves; $\alpha_1 = 0.001$ for the windward side of background waves. These values were determined through the comparison of RBCS calculated from radar backscatter theory with the *ERS-1/-2* scatterometer empirically based models CMOD3 and CMOD4. They are obtained from the study of Liu et al. (1997), as an improvement to the original values of Liu and Yan (1995). Liu et al. (1997) had considered both specular reflection and Bragg resonance in the calculation of the RBCS, Liu and Yan (1995) did not consider the contribution from specular reflection.

The MSS for upwind and crosswind can be calculated from

$$\sigma_{wu}^2(k) = \int_{k_p}^{k} k\,dk \int_{-\pi}^{\pi} \Phi_w(k, \phi) k^2 \cos^2\phi\, d\phi \quad \text{and} \tag{14}$$

$$\sigma_{wc}^2(k) = \int_{k_p}^{k} k\,dk \int_{-\pi}^{\pi} \Phi_w(k, \phi) k^2 \sin^2\phi\, d\phi, \tag{15}$$

respectively. Here $\Phi_w(k, \phi)$ is the spectrum of gravity–capillary waves, given by (12) and (13); k_p, the lower limit of integration, is the wavenumber at spectral peak of fully developed gravity waves. Figures 1a,b give the MSS components, calculated from (14) and (15), for six different wavenumbers. Figure 1a is for upwind the component and Fig. 1b is for crosswind component. The MSS corresponding to equilibrium spectrum of background gravity waves is not included here. The triangles denote the MSS, integrated up to 0.1 mm from (14). According to the laser slope gauge laboratory measurements of Jähne and Riemer (1990), the image slope gauge laboratory measurements of Klinke and Jähne (1992) and the field measurements of Klinke and Jähne (1995), the high-frequency dissipation length should be about 1 mm. The upper limit of the above integration is 0.1 mm, which is over the high-frequency dissipation length. So, this MSS together with MSS of background gravity waves can represent one that optical sensor can detect. The other symbols denote the MSS generated by gravity–capillary waves (background gravity waves are not included) up to Ka, Ku, X, and S bands, respectively. The MSS, integrated from (14) and (15) up to various bands (except visible band), can be modeled by

$$\frac{\sigma_{wu}^2}{\sigma_{wc}^2} = 2, \quad \text{and} \tag{16}$$

$$\sigma_w^2 = \sigma_{wu}^2 + \sigma_{wc}^2 = 0.000012 U_{10}^{2.1} \ln\left(\frac{k^2}{2.5 \times 10^4} + 1\right), \tag{17}$$

where σ_w^2 represents the MSS of gravity–capillary waves, generated by both wind-induced waves and parasitic waves. In Fig. 1, the dashed lines represent the MSS given by (16) and (17). For the visible band, we do not give a formula for simulation. The equations, (16) and (17), which simulate the MSS integrated from (14) and (15), are provided to denote various band-filtered MSS of gravity–capillary waves, rather than the background gravity waves.

3. MSS of gravity waves

The MSS of gravity waves up to a wavenumber k can be calculated from

$$\sigma_g^2 = \int_{k_p}^{k} \Phi_g(k) F(k) k^2 k\, dk, \tag{18}$$

where k_p is the wavenumber at spectral peak for fully developed waves, $k_p = g/(1.2U_{10})^2$ (Donelan and Pierson 1987). Because the contribution from the waves longer than those at spectral peak is negligibly small, k_p is selected as a low cutoff wavenumber. In (18), the the unidirectional wavenumber spectrum in equilibrium (or saturation) range, $\Phi_g(k)$, has been given by Phillips (1958) as

$$\Phi_g(k) = \beta_g k^{-4}, \tag{19}$$

where β_g is a constant. In (18), the low-pass filter $F(k)$ suggested by Apel (1994) is

$$F(k) = 1/1 + (k/k_{\text{ro}})^2, \tag{20}$$

where k_{ro} is the high-frequency roll-off wavenumber for background gravity waves. The MSS, calculated from (18), (19) and (20), is

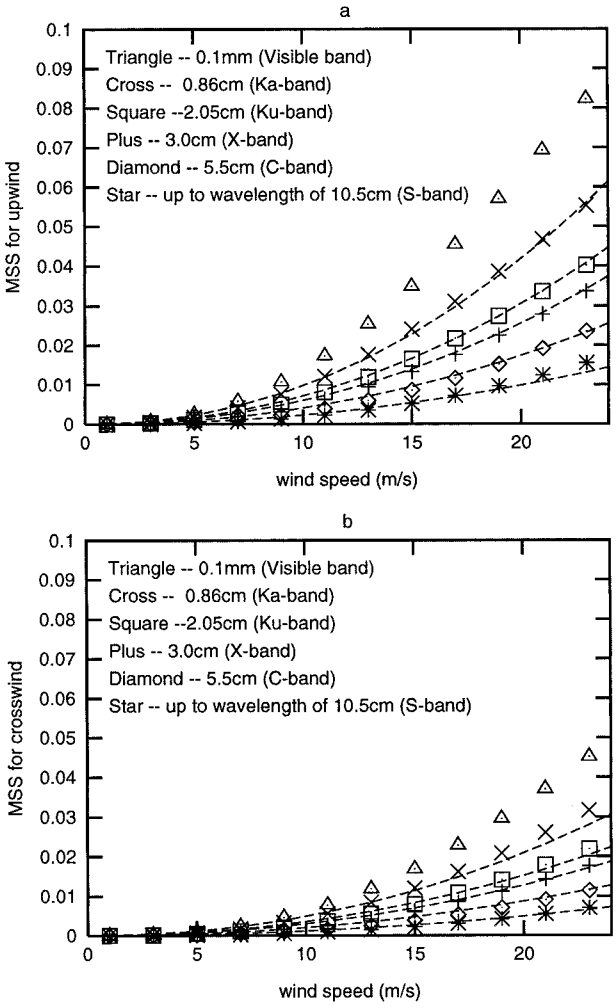

FIG. 1. The MSS of the gravity–capillary waves for six different bands. The dashed lines represent the MSS given by (16) and (17); the other symbols represent the MSS calculated from (14) and (15) (a) for upwnd direction and (b) for crosswind. The MSS corresponding to equilibrium spectrum of background gravity waves is not included here.

$$\sigma_g^2 = \frac{\beta_g}{2} \ln \frac{1 + \left(\frac{k_{ro}}{k_p}\right)^2}{1 + \left(\frac{k_{ro}}{k}\right)^2}. \tag{21}$$

Based on the laboratory measurements of Klinke and Jähne (1992), Apel (1994) suggested that $k_{ro} = 100$ rad m^{-1}. This value may need be adjusted for the open ocean. The values of β_g and k_{ro} can be determined from comparison of (21) with the observations of Cox and Munk (1954a,b). If we take the cutoff wavelength of a slick surface observed by Cox and Munk to be about 33 cm, we obtain $k_{ro} = 6\pi$ rad m^{-1} (i.e., $\lambda_{ro} = \frac{1}{3}$ m). Then, the constant β_g should be 0.0046, as suggested by Phillips (1977). The MSS up to $k = 6\pi$ rad m^{-1} (for a slick surface), calculated from Phillips' spectrum in the range from k_p to 6π, is

$$\sigma_g^2 = 0.0046(1 + 2 \ln U_{10}). \tag{22}$$

For radar backscatter and optical measurements, $k \gg k_{ro}$ and we have $k_{ro}/k \approx 0$. By comparing (21) with the observations of Cox and Munk (1954a,b), we select $\beta_g = 0.0046$ and $k_{ro} = 64$ rad m^{-1}. Substituting the values of β_g and k_{ro} into (21), we obtain

$$\sigma_g^2 \doteq \frac{0.0046}{2} \ln \frac{1 + \left(\frac{64}{k_p}\right)^2}{1 + 0} \doteq \frac{0.0046}{2} \ln \left(\frac{64}{k_p}\right)^2$$

$$= 0.0046 \ln \left(\frac{64}{k_p}\right); \tag{23}$$

substituting $k_p = g/(1.2U_{10})^2$ into (23), we have

$$\sigma_g^2 = 0.0103 + 0.0092 \ln U_{10}, \tag{24}$$

which represents the MSS of gravity waves for a clean surface. The bias between the MSS of a slick surface (22) and the MSS of a clean surface (24) is 0.0057, which is suitable to match the data when $U_{10} < 5$ m s^{-1} (Cox and Munk 1954a,b). In this range of wind speed, the MSS is almost totally contributed by gravity waves and the contribution from the gravity–capillary waves is negligibly small.

The MSS in (21) is not sensitive to the selection of β_g and k_{ro}. For example, when $k_{ro} = 30$ rad m^{-1} and $\beta_g = 0.0055$, the resulting MSS is very close to that of (24).

The ratio between MSS components of gravity waves for upwind and crosswind is

$$\frac{\sigma_{gu}^2}{\sigma_{gv}^2} = \frac{1.0}{0.9}, \tag{25}$$

which is obtained from the comparison of (22) and (24) with the observations of Cox and Munk (1954a,b).

In the above calculation, the low-frequency cutoff wavenumber is selected at the position of spectral peak, $k_p = g/(1.2U_{10})^2$, for simplicity. This sharp cutoff wavenumber means that we have ignored the contribution of waves longer than k_p on MSS. The MSS calculated from the Joint North Sea Wave Project spectrum (Hasselmann et al. 1973) in stage of full development, which has a smooth low-frequency roll-off wavenumber, was given in appendix B of Liu et al. (1997). The two expressions of MSS of gravity waves are very close to each other. This suggests that the error, generated by the cutoff wavenumber above, should be very small and could be ignored. More accurate estimate of MSS of gravity waves should involve in wave age, fetch, duration, and spectral width.

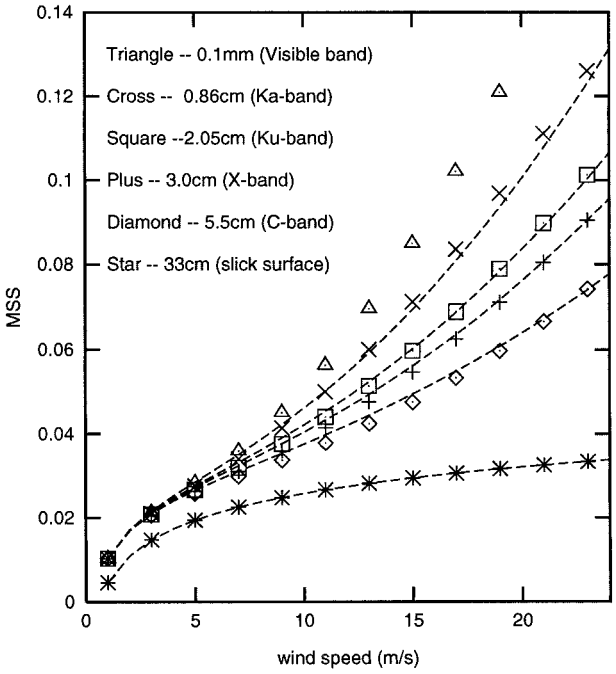

FIG. 2. The MSS of gravity waves and gravity–capillary waves for six different bands.

4. MSS in the entire wavenumber range

The probability theory has confirmed that the variance of sum of two independent random variables is equal to the sum of variances of these two variables. The MSS is the variance of ocean surface slope. The actual ocean surface slope is the sum of short-wave slope and underlying long-wave slope. The short-wave slope and the underlying long-wave slope are approximately independent on each other. The skewness of the ocean surface slope, generated by the correlation between the two slopes, is negligibly small (Liu et al. 1997). Therefore, the MSS up to various bands generated by both the gravity waves and the gravity–capillary waves, can be expressed as

$$\sigma^2 = \sigma_g^2 + \sigma_w^2, \tag{26}$$

where the MSS of gravity waves, σ_g^2, is given by (22) for a slick surface and by (24) for a clean surface. The MSS of gravity–capillary waves (including wind-induced part and parasitic part), σ_w^2, is given by (17). The MSS components for upwind and crosswind can be obtained from

$$\sigma_u^2 = \sigma_{gu}^2 + \sigma_{wu}^2 = \frac{1.0}{1.9}\sigma_g^2 + \frac{2}{3}\sigma_w^2, \tag{27}$$

$$\sigma_c^2 = \sigma_{gc}^2 + \sigma_{wc}^2 = \frac{0.9}{1.9}\sigma_g^2 + \frac{1}{3}\sigma_w^2. \tag{28}$$

Figure 2 shows the MSS for six wavenumbers. The discrete symbols denote the MSS integrated from (30). The triangles denote the MSS integrated up to 0.1 mm, which is over the high-frequency dissipation length. This MSS represents one that an optical sensor can detect. The other discrete symbols denote the MSS integrated up to Ka, Ku, X, C bands, and 33 cm (cutoff wavelength for a slick surface) using (30). The dashed lines denote the MSS given by (26), (22), (24), and (17). However, we do not give a formula to simulate MSS for the visible band.

5. Water wave spectra

The water wave spectra used to calculate the MSS in this study include the equilibrium spectrum of gravity waves and the spectrum of gravity–capillary waves. The spectrum of gravity–capillary waves includes the contributions from a wind-induced part and a parasitic part.

The water wave spectrum can be expressed as

$$\Phi(k) = \Phi_g(k)F(k) + \int_{-\pi}^{\pi} \Phi_w(k, \theta)\, d\theta, \tag{29}$$

where $\Phi_g(k)$ is the equilibrium (unidirectional) spectrum of gravity waves, given as (19) by Phillips (1958); $F(k)$ is the low-pass filter given as (20) by Apel (1994); and $\Phi_w(k, \theta)$ is the directional spectrum of gravity–capillary waves given by (12) and (13). The unidirectional MSS can be calculated from

$$\sigma^2 = \int_{k_p}^{k} \Phi(k)F(k)k^2 k\, dk, \tag{30}$$

where the spectrum model $\Phi(k)$ is provided by (29). The MSS components for upwind and crosswind can be obtained from

$$\sigma_u^2(k) = \frac{1.0}{1.9}\sigma_g^2 + \int_0^k k\, dk \int_{-\pi}^{\pi} \Phi_w(k, \phi)k^2 \cos^2\phi\, d\phi \tag{31}$$

and

$$\sigma_c^2(k) = \frac{0.9}{1.9}\sigma_g^2 + \int_0^k k\, dk \int_{-\pi}^{\pi} \Phi_w(k, \phi)k^2 \sin^2\phi\, d\phi, \tag{32}$$

where σ_g is given by (24) for a clean surface or (22) for a slick surface.

Figure 3a shows the elevation spectrum (29); Fig. 3b gives the curvature spectrum corresponding to (29). The saturation constant in (19) is $\beta_g = 0.0046$, the high-frequency roll-off wavenumber in (20) is $k_{ro} = 64$ rad m^{-1}.

Figure 3b shows that the saturation range is between k_p and $10k_p$. For the short-gravity waves with wavenumber larger than $10k_p$, the energy level does not remain constant. The characteristics of the short-gravity waves for $k > 10k_p$ are little understood at present. Although (29) is only an approximate description for this range, it gives a smooth connection between the gravity waves in the saturation range and the wind-induced gravity–capillary waves. Equation (30) shows that the integration range for both Phillips' equilibrium

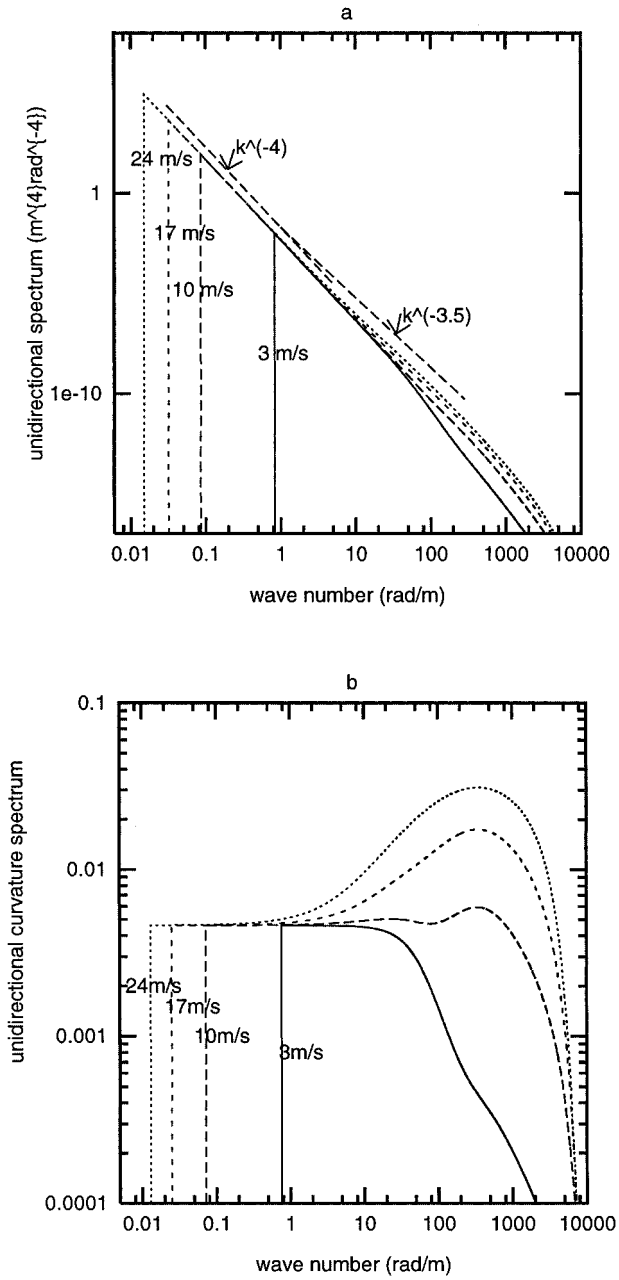

FIG. 3. (a) The elevation spectrum by (29) vs wavenumber. (b) The curvature spectrum corresponding to (29).

spectrum and our gravity–capillary wave spectrum is the same. This processing has no significance of dynamics and is only a method. As seen in Fig. 3, this processing may overestimate the MSS of ocean surface waves at high wind condition.

6. Comparison with other investigations

The MSS integrated up to 0.1 mm from (29) corresponds to one detected by optical instruments. Figure 4 gives comparison of the integrated MSS with the optical observations of Cox and Munk (1954a,b) for a clean surface and a slick surface, respectively. The total MSS generated by both gravity–capillary waves and underlying gravity waves is shown in Fig. 4a. The component for upwind is shown in Fig. 4b and for crosswind in Fig. 4c. Figure 4 shows that the MSS integrated up to 0.1 mm (or any a wavelength between 1 mm and wavelength of visible light) from (31) and (32) and spectrum model (29) can well fit the MSS detected by optical measurements. Figures 4b,c also show that the ratio between σ_u^2 and σ_c^2 is correct.

The MSS in (26), (27), and (28) will be used to represent the MSS of the ocean surface up to various microwave radar bands. Figure 5 gives a comparison of X band ($\lambda = 2.5$ cm or $k = 251$ rad m^{-1}) filtered MSS in (26) with the MSS by Wu (1994) for X band and the MSS averaged by Apel (1994) based on the radar backscatter measurements of C, X, Ku, and Ka bands. Figure 5 shows that our MSS is consistent with Wu for $U_{10} < 7$ m s^{-1}, and approximately consistent with Apel when $U_{10} > 7$ m s^{-1}.

Figure 6 gives a comparison of the RBCS, calculated from theoretical formula (8) or (9) using the Ku-band ($k = 287$ rad m^{-1}) filtered MSS, given by (27) and (28), with the empirically based Ku-band models of Witter and Chelton (1991) for the Geosat altimeter of 13.5 GHz ($k = 283$ rad m^{-1}), and Brown (1981) for the *GOES-3* altimeter of 13.9 GHz ($k = 291$ rad m^{-1}). In Fig. 6, the solid line represents the RBCS calculated from (8) and the dashed line represents the RBCS calculated from (9). The effect of peakedness is shown by the dashed line. In the calculation of (9), the peakedness coefficient n is taken to be 10, based on the comparison with the Gram–Charlier distribution of Cox and Munk (1954a,b) in the range of small slope (Liu et al. 1997). This figure shows that the proposed MSS for Ku-band wavenumber is suitable to interpret altimeter measurements. Figures 7a,b give comparisons of the RBCS, calculated from radar backscatter theory (both specular reflection and two-scale Bragg resonance) using C-band ($k = 111$ rad m^{-1}) filtered MSS in (27) and (28), with the empirically based models CMOD3 and CMOD4 (Rufenach 1995; Liu and Yan 1995) for *ERS-1/-2* scatterometer of 5.3 GHz ($k = 111$ rad m^{-1}) in upwind and crosswind directions, respectively. The dashed lines represent the RBCS due to only specular reflection; the solid lines represent the RBCS due to both specular reflection and two-scale Bragg resonance. The specular reflection is directly related to the MSS of the ocean surface. The Bragg resonance is proportional to the spectrum of short waves in the corresponding range. A discrepancy between the theoretical RBCS and empirical CMOD3 and CMOD4 is present in the range of $\theta > 30°$. It reflects the uncertainty of short-wave spectrum due to wave–drift interaction. For $\theta < 30°$, the proposed MSS is suitable to predict RBCS from specular reflection the-

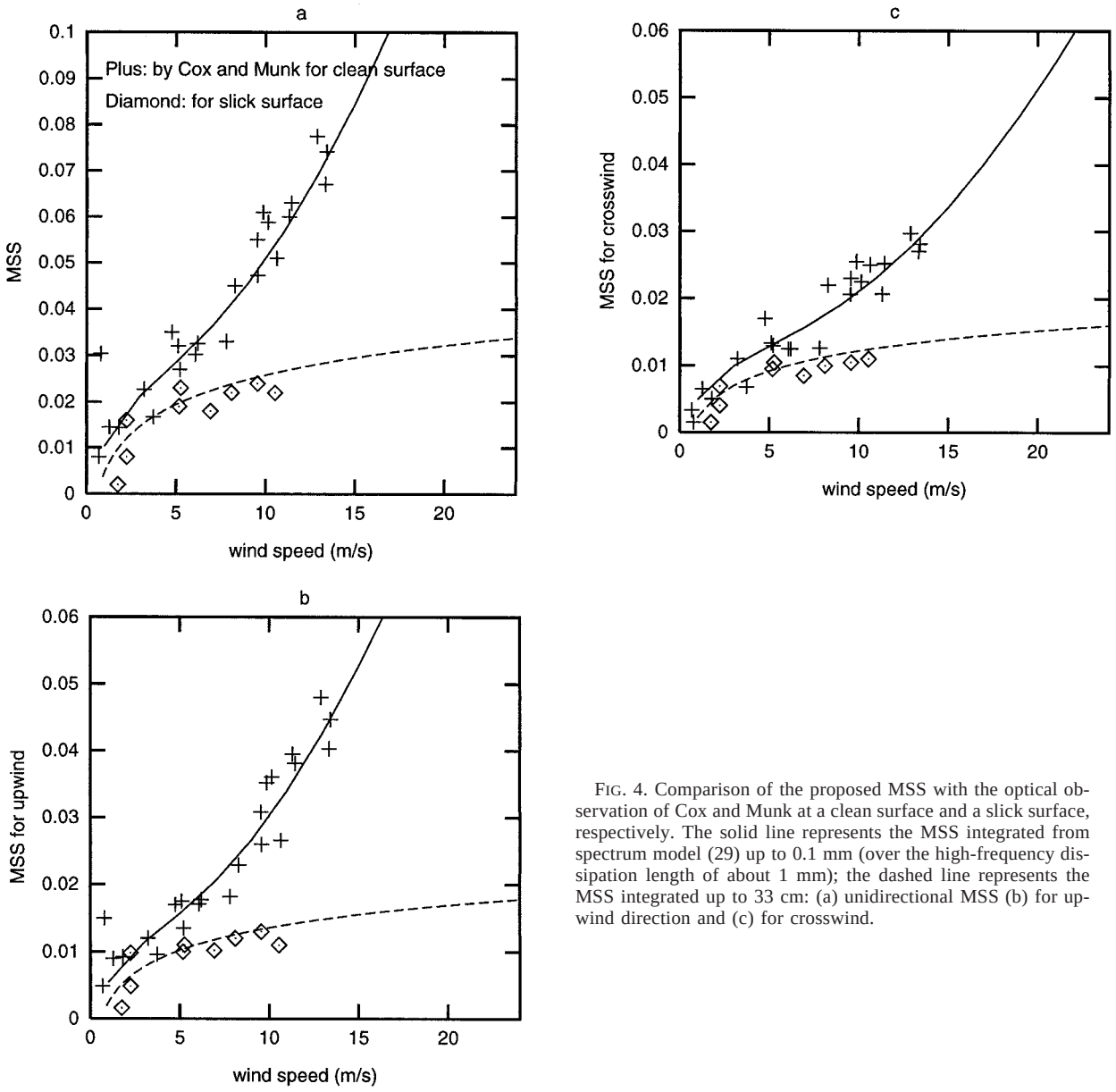

FIG. 4. Comparison of the proposed MSS with the optical observation of Cox and Munk at a clean surface and a slick surface, respectively. The solid line represents the MSS integrated from spectrum model (29) up to 0.1 mm (over the high-frequency dissipation length of about 1 mm); the dashed line represents the MSS integrated up to 33 cm: (a) unidirectional MSS (b) for upwind direction and (c) for crosswind.

ory. For the proper selection of the peakedness coefficient n, see Liu et al. (1997).

7. Involved physics and arguments

a. Physics on parasitic capillary waves

Although the spectrum model expressed by (12) and (13) was derived based on our understanding of the physics on wind-induced short waves with free traveling, it is empirically found that this model can also somewhat describe the parasitic capillary wave spectrum. In this section, we will discuss the physical seasons.

First, why does the molecular viscosity of capillary waves disappear in the spectrum model?

For parasitic capillary waves, we know

$$c = u_0 = C - A\Omega \cos\theta, \tag{33}$$

where c is the phase speed of the parasitic capillary waves, u_0 is the current velocity generated by the underlying waves, C is the phase speed of the underlying waves, $A\Omega$ is the amplitude of the underlying wave orbital velocity, and θ is the phase angle of the orbital velocity. This formula has been used by Longuet-Higgins (1963) and Phillips (1977). As indicated by them, the local phase speed c is equal to the speed of the opposing current u_0, the sum of the phase speed C and

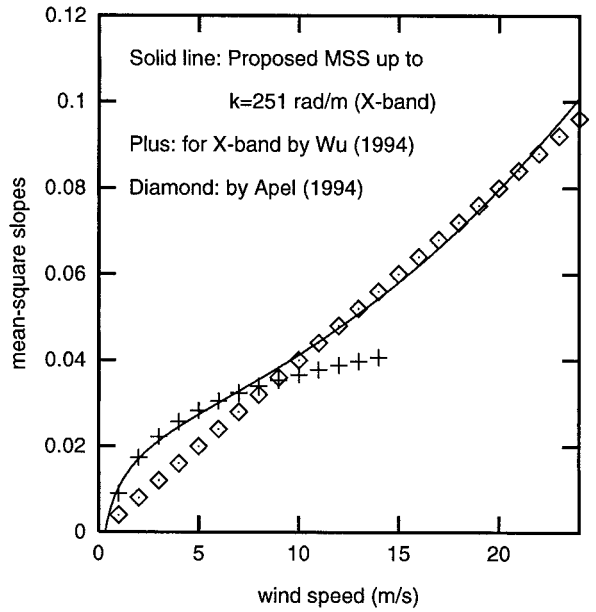

FIG. 5. Comparison of the X-band ($k = 251$ rad m^{-1} and $\lambda = 2.5$ cm) filtered MSS, obtained from (26) with the results of Wu (1994) and Apel (1994).

particle velocity near the long wave crest. Under this condition the parasitic capillary waves are stationary (Zhang 1995). Longuet-Higgins (1963) and Phillips (1977) focussed on pure parasitic capillary waves generated by sharp crest or increased local curvature. We focus on the wind-induced parasitic capillary waves. The wind-induced parasitic capillary waves may stand at any position of underlying waves, if (33) is satisfied. It means that the value of θ in (33) may be positive, negative, or zero. The wind-induced capillary waves must ride on other waves with condition of (33), otherwise the molecular viscosity can kill them very soon. It is not difficult for a wind-induced capillary wave to find a place with condition of (33). Every underlying wave has a position with satisfaction of (33).

With the condition of (33), the wind-induced capillary waves become parasitic. The molecular viscosity increases dramatically for shorter capillary waves. However, the energy consumption is continuous and mod-

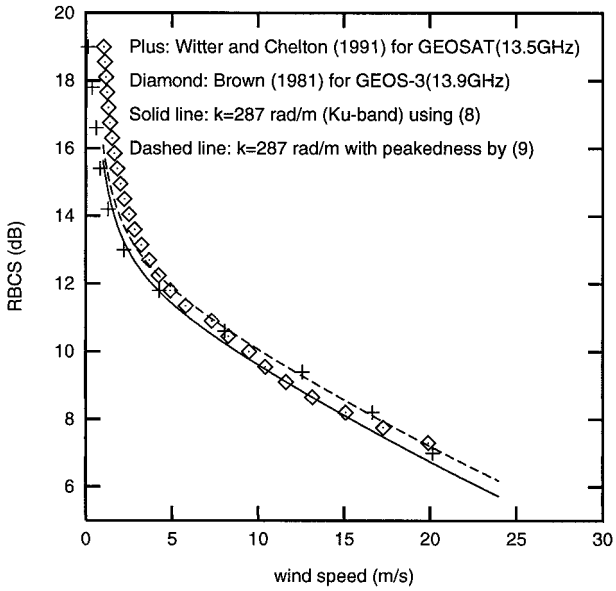

FIG. 6. The radar backscatter cross section (RBCS in dB) vs wind speed. The solid line represents the RBCS calculated from (8). The dashed line represents the RBCS calculated from (9) with the effect of peakedness. The proposed MSS for $k = 287$ rad m^{-1} (Ku band) is used to predict the RBCS at normal incidence. The frequency of Geosat altimeter is 13.5 GHz, which corresponds to a wavenumber of 283 rad m^{-1}. The frequency of *GEOS-3* altimeter is 13.9 GHz, which corresponds to a wavenumber of 291 rad m^{-1}.

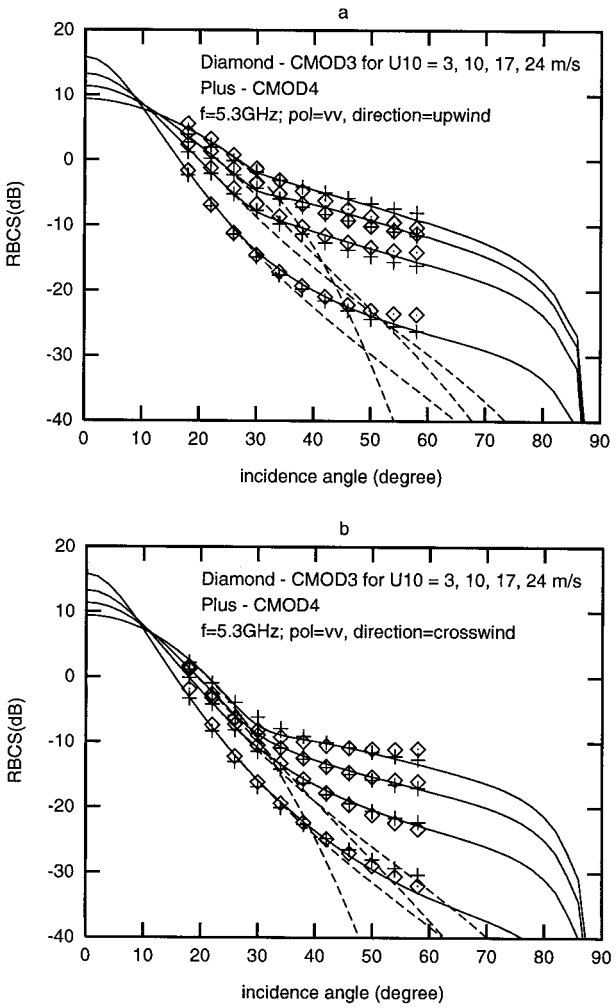

FIG. 7. The radar backscatter cross section (RBCS in dB) for vertically polarized 5.3-GHz C-band radar as a function of incidence angle with wind speed as a parameter. The solid lines represent the calculated RBCS due to both Bragg resonance and specular reflection using the proposed MSS in (27) and (28) for $k = 111$ rad m^{-1} and the PDF given by Liu et al. (1997). The dashed lines represent the calculated RBCS due to specular reflection only (a) for upwind direction and (b) for crosswind direction.

erate, not intermittent and violent. For this type of dissipation, the underlying waves have the ability to counteract the dissipation. The consumption due to molecular viscosity of capillary waves is significant but ignorable for the underlying waves. Therefore, molecular viscosity does not influence the spectrum of parasitic capillary waves, but it does influence the spectrum of the gravity–capillary waves with free traveling. The effect of molecular viscosity on wave spectrum can be denoted by the threshold wind friction velocity δ. Based on the observation of wave growth rate by Larson and Wright (1975), Liu and Yan (1995) found that

$$\delta = 0.8(\text{cm s}^{-1}) + 1.1\ (\text{cm}^2\ \text{s}^{-1})k, \qquad (34)$$

where the unit of wavenumber k is in radians per centimeter. From (34), we know that the threshold wind friction velocity for the waves which the C-band radar can detect is about 3 cm s^{-1}, the threshold friction velocity for the waves which Ku-band radar can detect is about 5 cm s^{-1}. For simplicity, we select $\delta = 5$ cm s^{-1} in this study. This threshold friction velocity is also required for spectrum of parasitic waves, since the parasitic waves depend on the spectral level of underlying waves. The underlying waves include both the activest gravity–capillary waves with δ of 3–5 cm s^{-1}, and the short gravity waves, which obtain energy from the most active gravity–capillary waves. Therefore, both the parasitic capillary waves and short gravity waves should have the threshold friction velocity similar to that of the most active gravity–capillary waves. Without the most active gravity–capillary waves, the capillary waves cannot find dependable underlying waves and hence cannot survive.

We use the threshold friction velocity δ to represent the molecular viscosity, because of the fluctuation of wind stress. The detail was illustrated by Liu and Yan (1995).

Second, why does the wave–drift interaction influence on the parasitic capillary waves?

In (12), the item $[1 - \exp(-c^2/\alpha_1 U_{10}^2)] = [1 - \exp(c^2/c_p^2)(1.2^2/\alpha_1)]$ denotes the modulation of wave–drift interactions in wind direction, where c_p is the phase speed of spectral-peak waves. Banner and Phillips (1974) proposed that the short gravity waves may break when the wind drift with a speed faster than the short gravity waves overpasses them. The wind drifts with a mean speed of about $0.035U_{10}$ may be augmented by the long gravity waves at the position near their crests. Liu and Yan (1995) obtained the same conclusion for gravity–capillary waves with free traveling. This mechanism can be denoted through the above item.

The formula (33) suggests that the wind-induced capillary waves may survive when they depend on their underlying waves as parasitic waves. Statistically, for the wind-induced capillary waves with phase speed c, the mean value of the phase speeds of their underlying waves should be $\overline{C} \doteq c$, and the mean value of the phase angles $\overline{\theta}$ should be zero.

Because of (33), not only can the molecular viscosity of the parasitic capillary waves be ignored but also their spectral modulation due to wave–drift interaction is controlled by the underlying waves. When the underlying waves break due to the drift–wave interaction, the parasitic capillary waves riding on them lose dependence. Without dependence, the capillary waves cannot survive because of serious molecular viscosity.

Combining the reasons illustrated in the above two paragraphs, we deduce that when wind drift overpasses a series of waves, the underlying waves break and the parasitic capillary waves riding on them lose dependence at the same time. Their travel speeds are the same. Statistically, their phase speeds are approximately the same. Therefore, we use the phase speed of capillary waves to replace that of underlying waves for describing the influence of underlying wave break on capillary wave spectrum.

The wave–drift interaction suppresses the gravity–capillary waves with free traveling directly and the parasitic capillary waves indirectly. Therefore, we use the above item to express the modulation of wave–drift interaction on the spectrum of entire wind-induced waves.

Third, why is the eddy viscosity of capillary waves significant?

The eddy viscosity D_e in (12) is based on turbulence dynamics, rather than classic dynamics. As introduced by Wen and Yu (1984), some Russian scientists in their early investigation attempted to calculate the mixing length of turbulence through the shearing of the orbital velocities of waves, further estimate the eddy dissipation, and did not have much success. This implies that the turbulence is not generated by the shearing of the orbital motion of waves. The turbulence is charactered by an eddy, which can be described by the vortex. The turbulence flow is generated by vortex bursting or ''breakup,'' according to the visualization observation of Kline et al. (1967), Corino and Brodkey (1969), and Kim et al. (1971). The eddy (or vortex) at the wind-drift layer is generated by discontinuity of horizontal wind drift, according to the theory of Prandtl (1952). The stress-producing turbulence motion is highly intermittent, occurring maybe about 25/100 times of the total time (Landahl and Mollo-Christensen 1992). The size of the eddy at drift layer is the same order as the thickness of wind–drift layer. Banner and Phillips (1974) observed a size of about 3–5 mm for the wind–drift layer at moderate wind condition. The eddy at the wind–drift layer can suck the significant part of short waves with a wavelength of millimeter order. The energy of short waves held by the eddy may be released into the water surface drift layer or deeper water layer through the vortex bursting. The suck itself does not consume the energy of short waves of millimeter wavelength, it only holds a part of the waves. The vortex bursting may bring water mass with the energy of short waves into the turbulence flow. All of the short waves that are being within the water mass or just passing here may lose

their energy. Limited by the eddy size, the eddy dissipation is significant only for shorter waves with millimeter-order wavelength. The high intermittence and the violent eddy breakup determine that this type of dissipation of capillary waves cannot be balanced by energy supply from their underlying waves. With serious loss of water mass and energy, these very short capillary waves are always deformed.

The cutoff point of high-frequency waves is found to be $k = 6280$ rad m^{-1} or $\lambda = 1$ mm (Apel 1994), where λ is the wavelength. This is consistent to our expression of the eddy viscosity in (13). The original expression of Liu and Yan (1995), obtained based on the image slope gauge laboratory measurement at 100-m fetch (Jähna and Riemer 1990), denotes a special case with more violent turbulence in the wind–drift layer, rather than a general condition.

Finally, why do we ignore the contribution from pure parasitic waves?

The sharp crest or increased local curvature of short-gravity waves may generate pure parasitic capillary waves, which are not induced by wind stress. The spectral peak at $k = 750$ rad m^{-1} shown by the measurements of Jähna and Riemer (1990) and Klinke and Jáhna (1992) may be due to the mechanics. This mechanics is not included in out model, because we consider that the contribution from this mechanics is significant only for very young waves. Their spectral peaks are located in the region of short gravity waves and cause high local curvature for significant part of the short gravity waves. For fully developed waves at moderate and strong wind conditions, the spectral peaks are far away from short gravity wave region. The possibility of sharp crest or high local curvature of short gravity waves is small, hence we ignore it. The error generated by this approximation exists.

b. c^2/c_p^2 dependence and k_p/k dependence

The spectrum of gravity–capillary waves, expressed by (12) and (13), is derived on a balance of the wind input, the spectral flux divergence, the viscous dissipation, and the modulation from the wave–drift interaction (Liu and Yan 1995). At first, this spectrum is proportional to the wind-induced wave growth rate normalized by the angular frequency, β/ω. The expression of normalized wave growth rate given by Plant (1982) is $\beta/\omega = 0.04(u_* - \delta)^2/c^2 \doteq 0.04(u_*/c)^2$. The threshold wind friction velocity δ was proposed by Liu and Yan (1995) based on the balance between molecular viscosity and wind stress fluctuation. In (12), the item $[1 - \exp(-c^2/\alpha_1 U_{10}^2)] = [1 - \exp(c^2/c_p^2)(1.2^2/\alpha_1)]$ denotes the modulation of wave–drift interactions in wind direction, where c_p is the phase speed of gravity waves at spectral peak and α_1 is the dissipation coefficients at upwind direction. Based on the theory of Banner and Phillips (1974), the tank measurements and the field measurements of remote sensing, it is found that the wave–drift interactions have the effect of suppressing the spectral energy at high wind condition. This effect can be described by the ratio between c^2 and c_p^2, rather than k_p and k. This effect is present in both the upwind spectrum and the directional spreading function. Two coefficients, α_1 and α_2, are used to describe the extent of wave–drift interactions. In this study, these coefficients are determined from the comparison of the theoretical RBCS with the *ERS-1/-2* scatterometer models CMOD3 and CMOD4. These two empirically based models were obtained from numerous data at open ocean (Liu and Yan 1995), hence they represent a state of statistical average. Such a statistical average generally corresponds to the neutral atmosphere and the fully developed waves. Therefore, the spectral model, (12) and (13), is for the same atmosphere and wave age conditions.

The most significant contribution, included in (12) and (13), is that both the upwind spectrum and the directional spreading rate are controlled by $(c/c_p)^2$, rather than k_p/k. The observations for gravity waves (Donelan et al. 1985; Banner 1990) have confirmed the effect of the k_p/k ratio. According to our investigation in another manuscript, the variance of directional spreading rate of gravity waves near spectral peak is generated by another mechanics and can be described by k_p/k. The variance of directional spreading rate of gravity–capillary waves, generated by the wave–drift interaction, are controlled by $(c/c_p)^2$. Two types of dependence correspond to different mechanics and different range of wavenumber. The relationship of $(c/c_p)^2$ dependence of gravity–capillary waves was found by Liu and Yan (1994), and physically illustrated by Liu and Yan (1995) and Liu (1996). If one simply extends the relationship of k_p/k dependence into the range of shorter capillary waves, a too wide directional spreading rate will be obtained. Such a wide spreading would result in an overestimate of MSS.

For example, both the upwind spectra of Apel (1994) and Liu and Yan (1995) have similar spectral level. However, Apel (1994) extended the k_p/k dependence developed by Donelan et al. (1985) and Banner (1990) from the range of the gravity waves into the range of gravity–capillary waves, even into the range of capillary waves. So, his spectrum in the range of capillary waves has a very wide spreading, which results in an overestimate of the MSS. The MSS calculated Apel (1994) is about two times greater than the observations of Cox and Munk (1954a,b), just due to the k_p/k dependence. The basic spreading of $\mathrm{sech}^2(h\phi)$ in our model is generated by the wind stress input. In (12) and (13), the wind–drift modulation changes both the directional spreading through (13) and the upwind spectrum through (12). The widest spreading of our spectrum is in the region near $k = 361$ rad m^{-1}, activest wind-induced waves. However, this wide spreading is generated by suppressing the spectrum level especially the upwind spectrum level, rather than increasing the di-

rectional spreading rate of wind stress input. Therefore, the MSS calculated can match the observation of Cox and Munk, although with some uncertainties at high wind condition.

c. $(u_*/c)^2$ dependence and u_*/c dependence

The dependence of $(u_*/c)^2$ on the spectrum of gravity–capillary waves in (12) is supported by both laboratory measurements and field remote sensing. The linear wind speed dependence of short gravity waves was proposed by Phillips (1985), based on the laboratory observations on frequency spectrum by Toba (1973). The linear wind speed dependence results in a relationship of $k^{-3.5}$ in the elevation wavenumber spectrum. However, Toba did not estimate the error generated by Doppler effect. Later observations on wavenumber spectrum differ from the result of Toba (1973). For example, all of the laboratory measurements using advanced optical technology (Jähne and Riemer 1990; Klinke and Jähne 1992; Hwang et al. 1993; Zhang 1995) support the relationship of nonlinear wind speed dependence of gravity–capillary wave spectrum. The spectrum models developed by Plant (1986), Donelan and Pierson (1987), Apel (1994), Liu and Yan (1995), and Elfouhaily et al. (1997) have denoted the nonlinear wind speed dependence. The scatterometer measurements also indirectly support the wind speed square dependence (Plant 1986; Donelan and Pierson 1987; Liu and Yan 1995; Liu et al. 1997).

Until now, only few spatial measurements of gravity–capillary waves in the field have been performed (Lee et al. 1992; Hara et al. 1994; Hwang et al. 1996; Klinke and Jähne 1995). The discrepancy between the curvature spectra from the above field measurements is about 10 times greater than the order of the lower one. As indicated by Klinke and Jähne (1995), the first three systems used impose severe limitations on the resolution. Because of lower two-dimensional (2D) resolution, the 2D spatial structure of the waves cannot be revealed. Limited by 2D low-wavenumber resolution, Hwang et al. (1996) had to calculate the transect wavenumber spectra from the field data sampled from a 10×6 cm^2 square outline. The transect wavenumber spectrum is the estimate using a one-dimensional (1D) analysis technique, rather than a 2D technique. The discrepancy between the transect spectrum and the unidirectional wavenumber spectrum (integrated over all propagation angles) can be calculated from a false random series generated by a known 2D signal and using a 1D analysis technique. An unpublished calculation of Dr. Y. Liu indicated that the discrepancy would be dramatically increased, when the directional spreading of the known signal widens. If the directional spreading of the signal is $\mathrm{sech}^2(1.3\phi)$, the discrepancy will be the six times greater than the original signal. Although the transect wavenumber spectrum obtained by Hwang et al. (1996) shows linear wind friction velocity dependence, it does not mean that the unidirectional wavenumber spectrum does also.

d. Other spectrum models published recently

Both the directional spreading function by Caudal and Hauser (1996) and the unified directional spectrum by Elfouhaily et al. (1997) have some common characteristics with our model, as expressed by (12) and (13). Based on radar backscatter theory, multifrequency radar measurements and the spectrum model at upwind direction by Apel (1994), Caudal and Hauser (1996) inferred a directional spreading function for the short wave spectrum. In their model, a polynomial of $\log_{10}(k)$ and wind speed was designed. The six parameters in this polynomial were obtained based on the radar data, radar backscatter theory, and upwind spectrum of Apel (1994). In lower wavenumber range, the spreading rate of their directional function increases with wavenumber. In higher wavenumber range, the spreading rate decreases with wavenumber. This character is just the effect of $(c/c_p)^2$. However, the position of the widest spreading in their model differs from ours. It is because they used the upwind spectrum of Apel (1994). Obviously, the radar data require that they give up the relationship of k_p/k dependence in Apel's directional spreading function. A suitable polynomial of $\log_{10}(k)$ can simulate the $(c/c_p)^2$ dependence.

The spectrum model for long and short waves given by Elfouhaily et al. (1997) is very close to our model. The unidirectional curvature spectrum shown in their Fig. 8b is very similar to ours in Fig. 3b. The reasons are as follows. 1) They adopt a c/c_p rather than k_p/k dependence to describe the directional spreading function of short waves. 2) They design a wide spreading function, which is equivalent to $\mathrm{sech}^2(1.3\phi)$ in our model. 3) They do not adopt the relationship of linear wind speed dependence. A two-regime logarithmic law is used by them to describe the curvature spectrum, based on the laboratory measurements of Jähne and Riemer (1990) and the field data of Hara et al. (1994).

e. Conditions

In this study, the derived MSS and the proposed spectrum model are in effect to fit field data of radar measurements and optical observations only for atmosphere condition of neutral stability and for the wave age of fully developed stage. The MSS of gravity waves is derived using a formula of $k_p = g/(1.2U_{10})^2$, which denotes the the peak wavenumber at fully developed stage. The influence of wave age on gravity wave spectrum has been investigated by Hasselmann (1973), Donelan et al.(1985), and others as cited by Elfouhaily et al. (1997). The wind friction velocity in this study is determined from the drag coefficient of Pierson et al. (1984), which is

$$C_d = 10^{-3}(2.717U_{10}^{-1} + 0.142 + 0.0761U_{10}). \quad (35)$$

The influence of atmospheric stability on drag coefficient was illustrated by Pierson (1990). The effect of atmospheric stability on slope was investigated by Hwang and Shemdin (1988), on vertical momentum flux by Ohya et al. (1997), and on wave growth by Voorrips et al. (1995).

For young waves, the spectral-peak wavenumber k_p increases. Under strong stable atmosphere condition, both the wind friction velocity and the directional spreading of wind input decrease. In these two cases, the MSS of ocean surface waves should be less than the normal.

f. Non-Gaussian PDF of slopes

According to Longuet-Higgins (1963) and Phillips (1977), the nonlinear wave–wave interactions can result in nonsinusoidal shape of surface waves and increase the skewness of surface elevations. The departure of elevations from the Gaussian distribution appears to be a statistical consequence of the tendency of the waves to form sharp crests and shallow troughs. According to the laboratory observations of Kinsman (1960) and Huang and Long (1980), the PDF of elevations within 2.5 times standard deviation can be described by the Gram–Charlier distribution with a skewness coefficient and a peakedness coefficient. According to the optical observations of Cox and Munk (1954a,b), the PDF of slopes within 2.5 times standard deviation can be described by the 2D Gram–Charlier distribution with two skewness coefficients and three peakedness coefficients.

Because of the high sensitivity of microwave radar, the RBCS due to specular reflection provides us with the possibility to accurately measure the probability of large slopes. Based on both probability theory and scatterometer measurements, Liu et al. (1997) derived a new PDF for sea surface slopes, as shown in (3). Their investigation suggested that the PDF of slopes within six times of the standard deviation cannot be described by the Gram–Charlier distribution given by Cox and Munk (1954a,b). The six times of the standard deviation is the range at which radar can detect through simple specular reflection theory. We do not doubt that the Gram–Charlier distribution with more items and more peakedness coefficients could describe the PDF of slopes with large values. The investigation of Liu et al. (1997) found that the peakedness (kurtosis) of slopes are also the statistical consequence of sharp crests and shallow troughs. Their paper suggests that the nonsinusoidal shape of waves with sharp crests and shallow troughs is generated by nonlinear wave–wave interactions in the range of gravity waves.

Figure 2 in this study shows that the MSS of gravity waves is much larger than that of shorter gravity–capillary waves in low wind conditions. So, the departure of slopes from the Gaussian distribution is more serious in low wind conditions. This consequence is in agreement with that shown in Fig. 7. In Fig. 7, it is found that the RBCS due to specular reflection plays a more significant role in low wind conditions where the incidence angles are less than 30°. The nonlinear wave–wave interactions are controlled by the spectral width parameter (Liu et al. 1997).

The long wave breaking significantly increases the probability of very large slopes beyond six times of the standard deviation. This has been observed by Lee et al. (1995, 1996) from the grazing-angle-dependent signals and their Doppler spectra. The long wave breaking and cresting give strongly reflecting facets at angles well beyond those predicated in simple specular-point theory, including out to grazing angles. Lee et al. (1995) found strong evidence that in low grazing angles, lifetime-dominated, non-Bragg scattering contributes noticeably to returns for both polarizations, but is dominant in providing return for the horizontal polarization. Without consideration of long wave breaking, our model on the PDF of slopes cannot accurately predict the returns of both polarizations at low grazing angles, especially for the horizontal polarization.

8. Summary

The MSS of the ocean surface is very important for understanding the physical processes at the air–sea interface, and for interpreting altimeter and scatterometer radar backscatter measurements. This study provides a formula for the MSS of the ocean surface at various radar wavenumbers based on the previous models of water wave spectra. The spectrum of gravity–capillary waves is obtained based on our understanding of the physical processes. The eddy-viscosity coefficient is determined from some of the laboratory measurement and field measurement (Jähna and Riemer 1990; Klinke and Jähna 1992, 1995). The other parameters of the spectrum model are determined through the comparison of RBCS calculated from radar backscatter theory with the *ERS-1/2* scatterometer empirically based models CMOD3 and CMOD4, rather than with laboratory measurements. The comparisons of derived MSS with the field measurements and various investigations confirm that the proposed MSS are approximately correct within the range concerned. The formula (17) is given for simulation of MSS of ocean surface waves up to any wavenumber under the Ka band and will provide convenience for the quantitative research on the ocean waves and the radar backscatter of the sea. However, the deviation of our estimates from real one may exist, especially under the condition of high wind, due to our little understanding of the connection between the long background gravity waves and the short gravity–capillary waves.

This study gives further explanations for the physics of gravity–capillary waves, which were not given by Liu and Yan (1995). For example, some questions are illustrated: 1) Why does the molecular viscosity of capillary waves disappear in the spectrum model? 2) Why does the wave–drift interaction influence on the parasitic

capillary waves? 3) Why is the eddy viscosity of capillary waves significant? 4) Why do we ignore the contribution from pure parasitic waves? The short wave dissipation due to wave–drift interactions has the effect of suppressing the spectral density at high wind condition, which does also influence on the directional spreading rate. This effect can be denoted by $(c/U_{10})^2$ or $(c/c_p)^2$ dependence. The k_p/k dependence can describe the upwind spectrum and spreading rate in the range of gravity waves, but it should not be extended to the region of short waves. Any attempt using k_p/k dependence to describe short wave spectrum will result in a too large MSS. In addition, the eddy viscosity for high-frequency waves has been illustrated based on turbulence at the wind–drift layer.

Acknowledgments. This research is supported partially by the National Science Foundation through Grant NSF-OCE 9453499, by the Office of Naval Research through Contract 73-6645-08, by the Earth Observing System (EOS) Interdisciplinary Science Investigation of the National Aeronautics and Space Administration (NASA), and by NASA Grant NAGS-7949.

REFERENCES

Apel, J. R., 1994: An improved model of the ocean surface wave vector spectrum and its effects on radar backscatter. *J. Geophys. Res.*, **99,** 16 269–16 291.

Banner, M. L., 1990: Equilibrium spectrum of wind waves. *J. Phys. Oceanogr.*, **20,** 966–984.

——, and O. M. Phillips, 1974: On the incipient breaking of small-scale waves. *J. Fluid Mech.*, **4,** 647–656.

Barrick, D. E., 1968: Rough surface scattering based on the specular point theory. *IEEE Trans. Antennas Propag.*, **AP-16,** 449–454.

Brown, G. S., 1981: The wind-speed measurement capability of spaceborne radar altimeters. *IEEE J. Oceanic Eng.*, **OE-6,** 59–63.

——, 1990: Quasi-specular scattering from the air–sea interface. *Surface Waves and Fluxes*, G. L. Geernaert and W. J. Plant, Eds., Vol. II, Kluwer Academic, 1–39.

Caudal, G., and D. Hauser, 1996: Directional spreading function of the sea wave spectrum at short scale, inferred from multifrequency radar observations. *J. Geophys. Res.*, **101,** 16 601–16 613.

Corino, E. R., and R. S. Brodkey, 1969: A visual investigation of the wall region in turbulent flow. *J. Fluid Mech.*, **37,** 1–30.

Cox, C. S., and W. H. Munk, 1954a: Measurement of the roughness of the sea surface from photographs of the sun's glitter. *J. Opt. Soc. Amer.*, **44,** 838–850.

——, and ——, 1954b: Statistics of the sea surface derived from sun glitter. *J. Mar. Res.*, **13,** 198–227.

Donelan, M. A., and W. J. Pierson, 1987: Radar scattering and equilibrium range in wind-generated waves with application to scatterometry. *J. Geophys. Res.*, **92,** 4971–5029.

——, J. Hamilton, and W. H. Hui, 1985: Directional spectra of wind-generated waves. *Philos. Trans. Roy. Soc. London*, **315,** 509–562.

Elfouhaily, T. B. Chapron, and K. Katsaros, 1997: A unified directional spectrum for long and short wind-driven waves. *J. Geophys. Res.*, **102,** 15 781–15 796.

Hara, T., E. J. Bock, and D. Lyzenga, 1994: In situ measurements of capillary–gravity wave spectra using a scanning laser slope gauge and microwave radars. *J. Geophys. Res.*, **99,** 12 593–12 602.

Hasselmann, K., and Coauthors, 1973: Measurements of wind-wave growth and swell decay during the the Joint North Sea Wave Project (JONSWAP). *Deutsches Hydrographisches Institut*, Hamburg, Reihe A, No. 12, 95 pp. [Available from Maury Oceanographic Library, Stennis Space Center, MS 39522-5001.]

Huang, N. E., and S. R. Long, 1980: An experimental study of the surface elevation probability distribution and statistics of wind-generated waves. *J. Fluid Mech.*, **101,** 179–200.

Hwang, P. A., and O. H. Shemdin, 1988: The dependence of sea surface slope on atmospheric stability and swell conditions. *J. Geophys. Res.*, **93,** 13 903–13 912.

——, D. B. Trizna, and J. Wu, 1993: Spatial measurements of short wind waves using a scanning slope sensor. *Dynamics of Atmospheres and Oceans*, Vol. 20, Elsevier Science, 1–23.

——, S. Atakturk, M. A. Sletten, and D. B. Trizna, 1996: A study of the wavenumber spectra of short water waves in the ocean. *J. Phys. Oceanogr.*, **26,** 1266–1285.

Jackson, F. C., 1991: Directional spectra from the radar ocean wave spectrometer during LEWEX. *Directional Ocean Wave Spectra*, R. C. Beal, Ed., The Johns Hopkins University Press, 91–97.

——, W. T. Walton, D. E. Hines, B. A. Walter, and C. Y. Pend, 1992: Sea surface mean square slope from K_u-band backscatter data. *J. Geophys. Res.*, **97,** 11 411–11 427.

Jähne, B., and K. S. Riemer, 1990: Two-dimensional wave number spectra of small-scale water surface waves. *J. Geophys. Res.*, **95,** 11 531–11 546.

Kim, H. T., S. J., Kline, and W. C. Reynolds, 1971: The production of turbulence near a smooth wall in a turbulent boundary layer. *J. Fluid Mech.*, **50,** 133–160.

Kinsman, B. 1960: Surface waves at short fetches and low wind speed—A field study. Chesapeaks Bay Institute, The John Hopkins University Tech. Rep. 19, 581 pp. [Available from Maury Oceanographic Library, Stennis Space Center, MS 39522-5001.]

Kline, S. J., W. G. Reynolds, F. A. Schraub, and P. W. Runstadler, 1967: The structure of turbulence boundary layer. *J. Fluid Mech.*, **30,** 741–773.

Klinke, J., and B. Jähne, 1992: 2D wave number spectra of short wind waves—Results from wind wave facilities and extrapolation to the ocean. *Optics of the Air–Sea Interface: Theory and Measurements*, L. Estep, Ed., International Society for Optical Engineering, 1–13.

——, and ——, 1995: Measurements of short ocean waves during the MBL ARI West Coast Experiment. *Air-Water Gas Transfer*, B. Jähne and E. C. Monahan, Eds., AEON Verlag & Studio, 165–173.

Landahl, M. T., and E. Mollo-Christensen, 1992: *Turbulence and Random Processes in Fluid Mechanics.* 2d ed. Cambridge University Press, 168 pp.

Larson, T. R., and J. W. Wright, 1975: Wind-generated gravity–capillary waves: Laboratory measurements of temporal growth rates using microwave backscatter. *J. Fluid Mech.*, **70,** 417–436.

Lee, P. H. Y., and Coauthors, 1992: Recent advances in ocean surface characterization by a scanning laser slope gauge. *Optics of the Air–Sea Interface: Theory and Measurements*, L. Estep, Ed., International Society for Optical Engineering, 234–244.

——, and Coauthors, 1995: X-band microwave backscattering from ocean waves. *J. Geophys. Res.*, **100,** 2591–2611.

——, J. D. Barter, K. L. Beach, E. Caponi, M. Caponi, C. L. Hindman, B. M. Lake, and H. Rungaldier, 1996: Wind-speed dependence of small-grazing-angle microwave backscatter from sea surface. *IEEE Trans. Antennas Propag.*, **44,** 333–340.

Liu, Y., 1996: The spectrum of gravity–capillary waves, the probability density function of ocean surface slopes and their effects on radar backscatter. Ph.D. dissertation, University of Delaware, 140 pp.

——, and W. J. Pierson, 1994: Comparisons of scatterometer models for the AMI on *ERS-1*: The possibility of systematic azimuth angle biases of wind speed and direction. *IEEE Trans. Geosci. Remote Sens.*, **32,** 626–635.

——, and X.-H. Yan, 1994: On the directional behavior of the

gravity–capillary waves. Abstract, *1994 Spring Meeting,* Baltimore, MD, Amer. Geophys. Union and Cosponsors, 196.

——, and ——, 1995: The wind-induced wave growth rate and the spectrum of the gravity–capillary waves. *J. Phys. Oceanogr.*, **25,** 3196–3218.

——, ——, W. T. Liu, and P. A. Hwang, 1997: The probability density function of the ocean surface slopes and its effects on radar backscatter. *J. Phys. Oceanogr.*, **27,** 782–797.

Longuet-Higgins, M. S., 1963: The generation of capillary gravity waves by steep gravity waves. *J. Fluid Mech.*, **16,** 138–159.

Masuko, H., K. Okamoto, M. Shimada, and S. Niwa, 1986: Measurement of microwave backscattering signatures of the ocean surface using *X* band and *K a* band airborne scatterometers. *J. Geophys. Res.*, **91,** 13 065–13 083.

Ohya, Y., D. E. Neff, and R. N. Meroney, 1997: Turbulence structure in a stratified boundary layer under stable condition. *Bound.-Layer Meteor.*, **83,** 139–161.

Phillips, O. M., 1958: Wavenumber range in the spectrum of wind-generated waves. *J. Fluid Mech.*, **4,** 426–434.

——, 1977: *The Dynamics of the Upper Ocean.* 2d ed. Cambridge University Press, 336 pp.

——, 1985: Spectral and statistical properties of the equilibrium range in wind-generated gravity waves. *J. Fluid Mech.*, **156,** 505–531.

Pierson, W. J., 1990: Dependence of radar backscatter on environmental parameter. *Surface Waves and Fluxes,* G. L. Geernaert and W. J. Plant, Eds., Vol. II, Kluwer Academic, 173–220.

——, W. B. Sylvester, and R. E. Salfi, 1984: Synoptic scale wind field properties from the SEASAT SASS. NASA Contractor Rep. 3810, Grant NAGW-266, 216 pp. [Available from Maury Oceanographic Library, Stennis Space Center, MS 39522-5001.]

Plant, W. J., 1982: A relationship between wind stress and wave slope. *J. Geophys. Res.*, **87,** 1961–1967.

——, 1986: A two-scale model of short wind-generated waves and scatterometry. *J. Geophys. Res.*, **91,** 10 735–10 749.

Prandtl, L., 1952: *Essentials of Fluid Dynamics with Applications to Hydraulics, Aeronautics, Meteorology and Other Subjects.* Hafner Publishing Company, 452 pp.

Rufenach, C., 1995: A new relationship between radar cross-section and ocean surface wind speed using *ERS-1* scatterometer and buoy measurements. *Int. J. Remote Sens.*, **16,** 3629–3647.

Schanda, E., Ed., 1976: *Remote Sensing for Environmental Sciences.* Springer-Verlag, 367 pp.

Toba, Y., 1973: Local balance in the air–sea boundary processes, 3, on the spectrum of wind waves. *J. Oceanogr. Soc. Japan,* **29,** 209–220.

Valenzuela, G. R., 1978: Theories for the interaction of electromagnetic and ocean wave—A review. *Bound.-Layer Meteor.*, **13,** 61–85.

Voorrips, A. C., V. K. Makin, and G. J. Komen, 1995: The influence of atmospheric stratification on the growth of water waves. *Bound.-Layer Meteor.*, **72,** 287–303.

Wen, S., and Z. Yu, 1984: *Wave Theory and Calculation Principle* (in Chinese). Science Press, 662 pp.

Witter, D. L., and D. B. Chelton, 1991: A Geosat altimeter wind speed algorithm and a method for altimeter wind speed algorithm development. *J. Geophys. Res.*, **96,** 8853–8860.

Wu, J., 1994: Altimeter wind and wind-stress algorithms—Further refinement and validation. *J. Atmos. Oceanic Technol.*, **11,** 210–215.

Zhang, X., 1995: Capillary–gravity and capillary waves generated in a wind wave tank: Observations and theories. *J. Fluid Mech.*, **289,** 51–82.